Hydrodynamic investigation on an OWC wave energy converter integrated into an OWT monopile

Yu Zhou[1], Dezhi Ning[1*], Wei Shi[1], Lars Johanning[1,2], Dongfang Liang[1, 3]

[1]State Key Laboratory of Coastal and Offshore Engineering, Dalian University of Technology, Dalian, 116024, China

[2] College of Engineering, Mathematics and Physical Sciences, University of Exeter, Penryn Campus, Penryn, Cornwall TR10 9FE, UK.

[3.] Department of Engineering, University of Cambridge, Cambridge, CB2 1PZ, UK

Abstract

Multi-functional platform is a promising way to enhance the economic power production from multiple renewable energy sources. This paper investigates numerically and experimentally the hydrodynamic performance of an oscillating water column (OWC) wave energy converter (WEC), integrated into a monopile-mounted offshore wind turbine (OWT). Based on linear potential flow theory, a 3D time-domain numerical model was developed, based on the higher-order boundary element method, to investigate the coupled hydrodynamic response of a cylindrical-type OWC device. A nonlinear pneumatic model was utilized to simulate the turbine damping. Experiments on the integrated system were carried out in a wave flume at Dalian University of Technology. The numerical results agree well with the experimental studies, including i) the surface elevation and air pressure inside the chamber, ii) wave pressure on the OWT monopile and iii) hydrodynamic efficiency. Furthermore, the effects of the OWC damping and wave steepness on the OWC-OWT system were investigated. It was found that the introduction of the OWC can significantly reduce the horizontal force and overturning moment on the OWT monopile, and that the wave steepness has a significant influence on the OWC efficiency, especially at resonance.

Keywords: Oscillating Water Column; OWT Monopile; Wave loads; HOBEM; Physical

* Corresponding author. Email address: dzning@dlut.edu.cn

Experiment.

Nomenclature

Notation

A Incident wave amplitude
b_w Thickness of the chamber wall
B Width of the flume
d Draft of the OWC chamber wall
d_c Air chamber height
$D=2R_2$ External diameter of the OWC chamber
D_o Turbine diameter
F Wave force
g Gravitational acceleration
G Green function
h Water depth
k Incident wave number
M Wave moment
$n = (n_x, n_y, n_z)$ Normal vector
$\overline{N_w}$ Average peak values of chamber surface-elevation, air pressure and efficiency
p Point pressure
p_s Source point
P_{air} Air pressure
$\triangle P$ Amplitude of the point pressure
$\triangle P_{air}$ Amplitude of the air pressure
P_{owc} Extracted wave power
P_{inc} Averaged incident wave energy
q_f Field point
Q Air volume flux
r_0 Inside radii of the damping layer
r_1 Outside radii of the damping layer
$1/R_0$ Rankine source
R_1 Radius of the OWT monopile
$1/R_z$ Image of Rankine source about the seabed
S Boundary surface
S_B Mean wet body surface
S_D Seabed
S_f Chamber cross-sectional area
S_{IF} Chamber free surface
S_{OF} Free surface outside the chamber
t Time

T	Incident wave period
u	Air flow velocity through the turbine orifice
$u_c(t)$	Normal vertical velocity of chamber free surface
(x_0, y_0, z_0)	Rotational center coordinates
z	Vertical coordinate
ω	Angular frequency
ρ	Water density
ϕ	Spatial potential
ϕ_i	Incident potential
ϕ_s	Scattered potential
η_s	Scattered wave elevation around the OWC
η_{crest}	Crest amplitude of the free surface
λ	Wave length
μ_1	Artificial damping coefficient
μ_2	Nonlinear pneumatic damping coefficient
$\nu_{(r)}$	Damping coefficient of the damping layer
α	Solid angle coefficient
ε	Opening ratio
$\overline{\sigma}$	Relative error
$\partial/\partial n$	Normal derivative on the solid surface
ξ	Hydrodynamic efficiency

1. Introduction

Offshore renewable energy is one of the most promising sources to address the climate change and the shortage of fossil fuels (Pechak et al., 2011). Various ocean energy are under consideration, including offshore wind, wave, tide range, marine currents and salinity gradients etc (Bahaj, 2011). Offshore wind turbine (OWT) technologies have seen a significant acceleration around the world, with the sector installing a record of 6.1GW in 2019 (Ohlenforst and Council, 2019). A large number of monopile offshore wind turbines have been constructed in the relatively shallow waters with depth smaller than 30 m (Achmus et al., 2009). By the end of 2018, monopiles remain the most popular foundation type, representing 81.9% of all installed foundations in Europe (Wind-Europe, 2019). As an offshore structure, the OWT monopiles are subject to not only aerodynamic loads from wind but also to hydrodynamic loads from wave and currents (Paulsen et al., 2019). Frequently re-occurring large wave loads can induce fatigue damage and lateral deformation of the structure elements and ground foundation (Slot et al., 2019). Hence, the OWT monopiles present one of the main design challenges related to the reliable operation and survivability (Wu et al., 2019). Conversely, wave energy also represents a potential energy resource with a higher power density than wind power (Sheng, 2019). The oscillating water column (OWC) wave energy converter (WEC) is a promising technology due to its simplicity and reliability (Heath, 2012; Falcão and Henriques, 2016). However, compared with solar and wind power devices, commercial exploitation of the OWC WECs is still limited as a source of electrical power device (Aemesto et al., 2014).

Combining the wind and wave energy converters together could be beneficial for utilizing the space and enhance energy extraction (Wan et al., 2015). It would also be beneficial for the wind and wave energy converters to share the infrastructures such as foundations, piles, power substations and cables etc to reduce the investment (Ren et al., 2018). In recent years, a lot of research have been carried out regarding the combined exploitation of the wave and offshore wind energy (Pérez-Collazo et al., 2015; Cheng et al., 2019). Sarmiento et al. (2019) performed an experimental study on a floating semi-submersible platform integrated with three OWC WECs under various wind, wave and current conditions. Michailides et al. (2016) carried out a physical model test to study the properties of a semi-submersible wind turbine combined with flap-type WECs. Haji et al. (2018) proposed a symbiotic design, including a standalone floating wind turbine and an OWC array, which has the potential to reduce the cost by 14% and increase the power production by 9%. Liang et al. (2017) investigated the hydrodynamic performance of a floating offshore floating renewable energy system, which integrates three types of renewable energy converters (wind, wave & current). The multiple system was found to reduce the dynamic response and increase the overall power production. Perez-Collazo et al. (2018) tested the hydrodynamic response of a hybrid wind-wave systems in an experimental campaign. Perez-Collazo et al. (2019) proved the feasibility of attaching an OWC device to the offshore fixed wind substructure. Following Perez-Collazo`s concept, this paper proposes an updated design of the integrated system. Fig. 1 shows the concept of the OWC device integrated into a fixed OWT monopile. A cylindrical chamber is placed around the OWT monopile to enable the OWC integration.

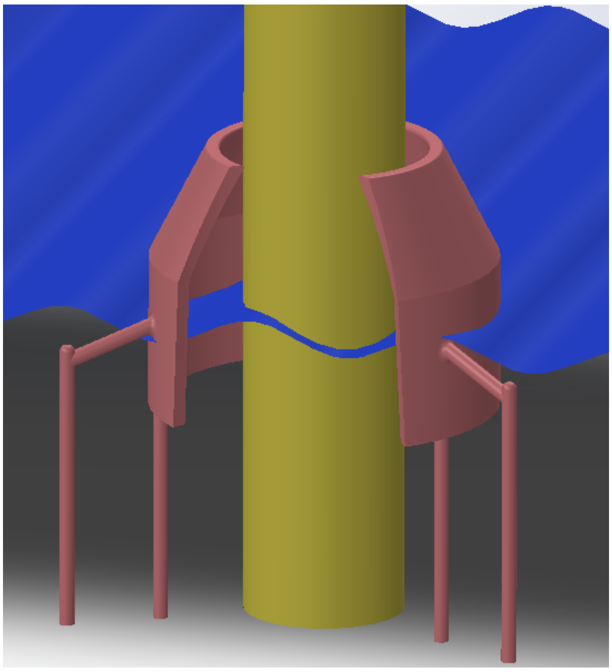

Fig. 1 Concept of the OWC device integrated into a fixed OWT monopile

The OWC device integrated into a floating supporter is another innovative design for capturing the wave energy from deep sea. A large number of researches have been conducted worldwide. Falcão et al. (2014) optimized and designed an axisymmetric Spar-buoy OWC device and the turbine damping system. A biradial impulse turbine was proved to be a better performance for the energy conversion. Gomes et al. (2016) simulated a heaving Spar-buoy OWC device to evaluate the effects of the side walls on the hydrodynamics of the device in a wave channel. Further, an experiment of floating Spar-buoy devices was also carried out for large-scale exploitation of the offshore renewable energy (da Fonseca et al., 2016). It was found that the array configuration performs a better performance than the isolated device. He et al. (2017) carried out a physical experiment to investigate the hydrodynamics of a dual pneumatic chambers OWC device installed on floating breakwaters. Elhanafi et al. (2017) investigated a 3D offshore OWC device subject to different wave amplitude and lip submergence. However, the motion of the floating device can counteract the OWC capability for capturing the wave energy. Compared with the floating device, the OWC integration into fixed offshore structures, such as breakwaters and OWT monopile, can perform higher efficiency and reliability due to motionless structure.

A number of models have been developed to design and optimize the OWC converters (Mahnamfar and Altunkaynak, 2017; Simonetti et al., 2017). The analytical method was applied for the preliminary design of the OWC devices (Ning et al., 2018). Zheng et al. (2018) investigated the interaction between a hybrid wave farm and the wave field by means of a semi-analytical model. Based on linear potential flow theory, He et al. (2019) developed an analytical model to study the hydrodynamics of a pile-supported OWC breakwater. Zheng et al. (2019) evaluated the effects of the array layout on the performance of the OWC devices based on an analytical solution. However, the analytical method can only be possible in special configurations, and it fails to capture the viscous loss and vortex shedding (Rezanejad et al., 2013). A large number of viscous-flow models based on the N-S equations have been developed to optimize the geometric parameters of the OWC devices (Elhanafi et al., 2017). A 3D CFD model has been constructed to investigate the impacts of power take-off (PTO) damping on the behaviour of a fixed Multi-Chamber OWC device (Shalby et al., 2019) and good agreement between numerical and experimental results was observed. Based on the RANS equations and the volume of fluid (VOF) method, Xu et al. (2016) considered a quadratic pressure loss coefficient to simulate a cylindrical OWC device in a wave flume. They found that the quadratic coefficient varies slightly with the wave period and wave height. However, viscous-flow models require a lot of computer resources (Chen et al., 2019). Based on the potential-flow theory, the higher-order boundary element method (HOBEM) has been applied to the OWC device (Koo and Kim, 2010). Wang et al. (2018) applied a time-domain HOBEM to simulate the nonlinear and viscous influences on a fixed OWC device, facilitated by experiments. Ning et al. (2019) carried out a fully nonlinear numerical simulation to cross-check the experimental results of a land-based dual-chamber OWC device.

This paper carries out numerical and experimental investigations on an OWC wave energy converter integrated into a fixed OWT monopile. It aims to simulate the hydrodynamic performance of the OWC device and the wave loads on the OWT monopile to prove the feasibility of the coupled OWC and OWT system. Section 2 presents the experimental model and the HOBEM model. The nonlinear pneumatic damping is introduced to represent the turbine. In section 3, the effects of the PTO damping and wave steepness on the hydrodynamics of the integrated system are discussed. Finally, the conclusions of this study are summarized in Section 4.

2. Experimental and numerical models

2.1. Experiment setup

A physical 3D model of the OWC integrated system, as shown in Fig. 2(a), was studied at a 1:20 scale in a wave-current flume at the State Key Laboratory of Coastal and Offshore Engineering in Dalian University of Technology. The flume is 60 m in length and 4 m in width, with a maximum water depth of 2.5 m. The single OWT monopile, as shown in Fig. 2(b), was also investigated for the comparative purpose. The model to be investigated was fixed at the center of the flume, as shown in Fig. 3. The water depth h was 1.0m in all cases. A Cartesian coordinate system Oxyz is defined with its origin at the center of the OWC. The radius of the OWT monopile R_1 is 0.1 m, and the external diameter of the OWC chamber is $D = 2R_2 = 0.8$ m. The effects of lateral flume walls can be ignored as discussed by Soares (1995) since $B/D \geq 5$, where B is the width of the flume. The draft of the OWC chamber wall d is 0.3 m. The thickness of the chamber wall was fixed to be $b_w = 0.1$ m. The air chamber height, i.e., the distance between the static water surface and the chamber ceiling, was set to be $d_c = 0.2$ m. In the scale-model experiment, the pneumatic air of the chamber can be considered ideal by ignoring the thermodynamic effects (Medina-Lopez et al., 2016). In order to simulate the effects of nonlinear turbine damping, a circular orifice, with a diameter $Do = 0.104$ m (Ning et al., 2020), is introduced at the position To (0m, 0m, 0.2m) as labelled in Fig. 3. The opening ratio ε (i.e., the ratio between the orifice area and the area of the internal OWC chamber) is 3.38%. In the present study, three LG1 type wave gauges, i.e., G_1–G_3, as shown in Fig. 3, were positioned to measure surface elevations along the centerline of the flume. Fig. 4(a) shows the wave gauges and the DS30 type acquisition system. Two CY200 type pressure sensors positioned at the top of the chamber, i.e. S_{a1} (0.11m, -0.11m, 0.2m) and S_{a2} (-0.11m, 0.11m, 0.2m), were used to record the air pressure at a sampling rate of 100 Hz. The 485-20 type acquisition system for the pressure sensors is shown in Fig. 4(b). In order to capture the pressure variations around the OWC system, twelve pressure sensors (S_1-S_{12}) were placed around the OWT monopile and the OWC chamber wall, as shown in Fig. 3. The positions of the pressure sensors are listed in Table 1.

(a) (b)

Fig. 2. Photographs of the experimental models (a) the OWC integrated system and (b) the OWT monopile.

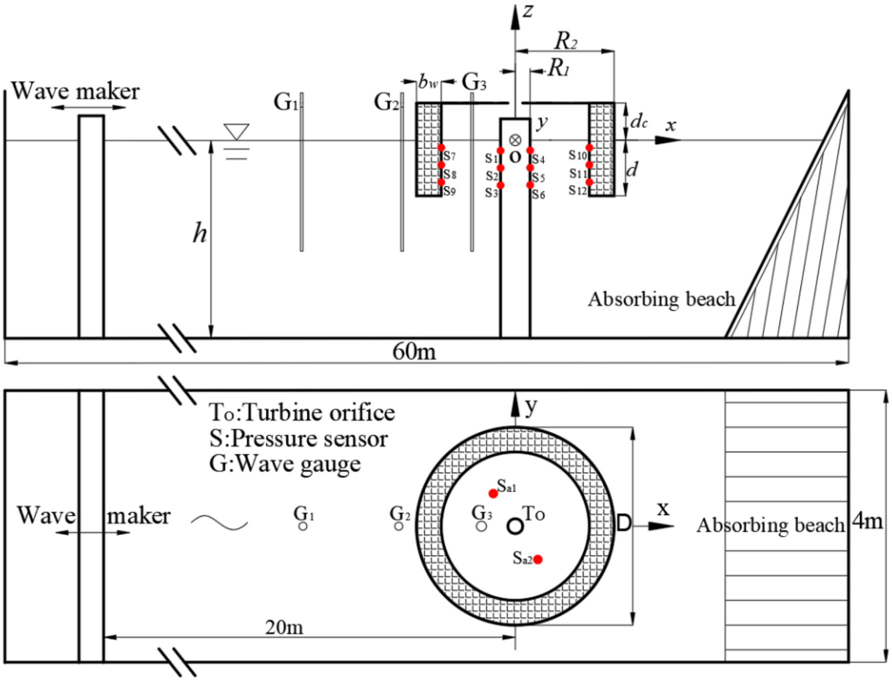

Fig. 3. Experiment layout. Top: a side view showing the OWC device, the wave gauges and the pressure sensors. Bottom: a plan view of the orifices and the air pressure sensors.

(a) Wave surface acquisition system (b) Pressure acquisition system

Fig. 4. The testing apparatus.

Table1 Positions of the pressure sensors.

	Position(m)		Position(m)		Position(m)		Position(m)
S_1	(-0.1, 0, -0.1)	S_4	(0.1, 0, -0.1)	S_7	(-0.3, 0, -0.07)	S_{10}	(0.3, 0, -0.07)

S_2	(-0.1, 0, -0.2)	S_5	(0.1, 0, -0.2)	S_8	(-0.3, 0, -0.17)	S_{11}	(0.3, 0, -0.17)
S_3	(-0.1, 0, -0.3)	S_6	(0.1, 0, -0.3)	S_9	(-0.3, 0, -0.27)	S_{12}	(0.3, 0, -0.27)

Table 2 Wave conditions for the tank test.

kh	3.33	2.81	2.6	2.42	2.26	2.11	1.99	1.87	1.68	1.53	1.2	1
(mm) (*kA*=0.05)	16.7	17.7	18.4	19.8	22.2	23.0	25.6	26.5	29.8	34.0	41.0	55.2
A (mm) (*kA*=0.075)	□	□	29.9	□	33.2	35.0	39.8	□	□	□	□	□
A (mm) (*kA*=0.10)	□	□	38.6	□	44.3	46.0	54.8	□	□	□	□	□
A(mm) (*kA*=0.15)	□	□	55.7	□	66.2	71.2	78.4	□	□	□	□	□

In the experiment, a series of monochromatic waves were generated in the wave-current flume to simulate the ocean waves, as listed in Table 2. The wave amplitude A varied with the wave number k, so as to obtain the desired wave steepness kA. In order to investigate the effect of the wave nonlinearity, four different wave steepness kA =0.05, 0.075, 0.10, 0.15 were considered as shown in Table 2.

In this study, the hydrodynamic efficiency of the OWC device can be calculated as the ratio between the pneumatic power and the power of the corresponding incident wave (Ning et al., 2015). The wave power extracted by the OWC device (i.e., P_{owc}) can be calculated by the time-average integration of the product of the air volume flux Q and chamber air pressure P_{air} (Morris-Thomas et al., 2007) as follows:

$$P_{owc} = \int_{S_f} \overline{P_{air}\left(t\right) \cdot Q\left(t\right)} dS = \frac{S_f}{T} \int_t^{t+T} P_{air}\left(t\right) \cdot u_c\left(t\right) dt \, , \tag{1}$$

where t denotes time, $u_c(t)$ is the normal vertical velocity of interior free surface. T denotes the period of the incident wave, S_f is the cross-sectional area of the free surface in the chamber.

The average energy flux per unit wave crest length P_{inc} is

$$P_{inc} = \frac{\rho g A^2 \omega}{4k}\left(1 + \frac{2kh}{\sinh 2kh}\right), \tag{2}$$

where ρ is the water density, g the gravitational acceleration and ω is the angular frequency that can be determined according to the wave dispersion equation $\omega^2 = gk\tanh(kh)$.

Therefore, the hydrodynamic efficiency can be defined as:

$$\xi = \frac{P_{owc}}{P_{inc} \cdot 2(R_2 - b_w)}, \tag{3}$$

2.2. Numerical model

Based on linear potential-flow theory, a 3D time-domain HOBEM was applied to investigate the hydrodynamic performance of the OWC integrated system. Fig. 5(a) shows the numerical setup of the OWC integrated system. The system can be considered as a concentric cylindrical model. A Cartesian coordinate system *Oxyz* is defined in the same way as in the experimental model shown in Fig. 3. It is assumed that the fluid is incompressible, inviscid and the motion is irrotational. The wave field around the device can be described by a complex spatial potential $\phi(x, y, z, t)$, which satisfies the Laplacian equation. Following the perturbation expansion procedure, the spatial potential ϕ can be divided into a known incident potential ϕ_i and an unknown scattered potential ϕ_s. The scattered potential ϕ_s satisfies the Laplacian equation:

$$\nabla^2 \phi_s(x, y, z, t) = 0, \tag{4}$$

The scattered potential is subject to the impermeable condition at the bottom S_D and the solid body surface S_B:

$$\frac{\partial \phi_s}{\partial n} = -\frac{\partial \phi_i}{\partial n}, \text{ on } S_D \text{ and } S_B \tag{5}$$

where $\partial/\partial n$ denotes the normal derivative on the solid surface. In order to analyze the wave motion in a finite domain, a sponge layer is introduced to absorb the reflected waves from the device (Ferrant, 1993), as shown in Fig. 5(b). To simulate the viscous loss and vortex shedding, a linear damping term is included on the free surface dynamic boundary condition inside the chamber (Kim, 2003). Following the Taylor expansion, the kinematic and dynamic boundary conditions on the free surfaces S_{IF} and S_{OF} can be expressed as (Ning et al., 2016):

$$\begin{cases} \dfrac{\partial \eta_s}{\partial t} = \dfrac{\partial \phi_s}{\partial z} - \nu_{(r)} \eta_s \\ \dfrac{\partial \phi_s}{\partial t} = -g\eta_s - \dfrac{P_{air}}{\rho} - \mu_1 \dfrac{\partial \phi}{\partial n} - \nu_{(r)} \phi_s \end{cases}, \tag{6}$$

where η_s denotes the scattered wave elevation around the device, μ_1 is the artificial damping coefficient and $\nu_{(r)}$ is the damping coefficient of the damping layer. The second and third terms in the right-hand side of dynamic condition, represent the pneumatic pressure and the viscous effects induced by the OWC shell, respectively. These two terms are only considered inside the OWC chamber. The damping coefficient $\nu_{(r)}$ can be expressed as:

$$\nu_{(r)} = \begin{cases} \omega \left(\dfrac{r - r_0}{\lambda} \right)^2 & r_0 \le r \le r_1 = r_0 + \lambda \\ 0 & r < r_0 \end{cases}, \tag{7}$$

where λ is the wave length, r_0 and r_1 are the inside and outside radii of the damping layer respectively. The air pressure P_{air} can be linked to the square of the flow velocity (Sheng et al., 2013):

$$P_{air}(t) = \mu_2 \left| u(t) \right| u(t), \tag{8}$$

where u is the air flow velocity through the circular orifice, μ_2 is the nonlinear pneumatic damping coefficient which characterizes the turbine damping. Both μ_1 and μ_2 can be determined with the trial and error technique by matching the numerical predictions with the experimental measurements.

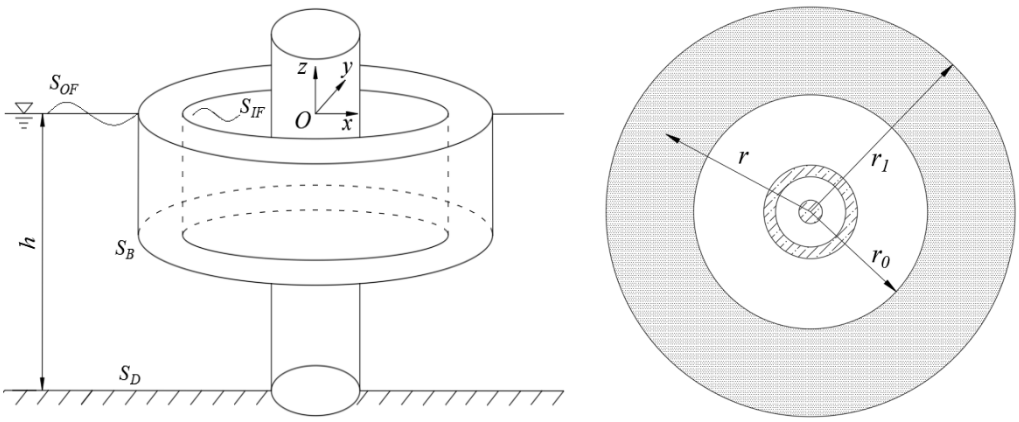

(a) (b)

Fig. 5. Computational model: (a) the sketch of the OWC integrated model, (b) the illustration of the sponge layer.

The Green's second identity can be applied to the above boundary value problem with the Rankine source and its image about the seabed as the Green function (Bai and Teng, 2013).

$$G\left(p_s, q_f\right) = -\frac{1}{4\pi}\left(\frac{1}{R_0} + \frac{1}{R_z}\right), \tag{9}$$

where $p_s = (x_1, y_1, z_1)$ and $q_f = (x, y, z)$ are the source point and the field point, respectively, and

$$\begin{cases} R_0 = \sqrt{\left(x - x_1\right)^2 + \left(y - y_1\right)^2 + \left(z - z_1\right)^2} \\ R_z = \sqrt{\left(x - x_1\right)^2 + \left(y - y_1\right)^2 + \left(z + z_1 + 2h\right)^2} \end{cases}, \tag{10}$$

Then, the integral equation for the scattered wave can be obtained:

$$\alpha\phi_s\left(p_s\right) = \iint_S \left[\phi_s\left(q_f\right)\frac{\partial G\left(q_f, p_s\right)}{\partial n} - G\left(q_f, p_s\right)\frac{\partial \phi_s\left(q_f\right)}{\partial n}\right] dS, \tag{11}$$

where the boundary surface S includes the mean free surface (S_{OF} and S_{IF}) and the solid surface, α is the solid angle coefficient. A higher-order boundary element method is used to solve the boundary integral equation numerically. In the time domain, the simulation is advanced using the fourth-order Adams-Bashforth predictor-corrector method to predict the free surface and potential. The detailed procedure is referred to Jin et al. (2017). After solving Eq. (11), the spatial potential around the OWC integrated system can be obtained. According to following the Bernoulli equation, the pressure inside the OWC integrated system can also be obtained:

$$p(t) = -\rho\frac{\partial \phi}{\partial t} + P_{air}(t), \tag{12}$$

The second term at the right side in Eq.(12) will be neglected if the single OWT monopile without OWC integration is considered.

The wave force and moment on the OWT monopile can be calculated by integrating the pressure over the wet surface of the inner cylinder:

$$F = \iint\limits_{S_{monopile}} pndS\,, \tag{13}$$

$$M = \iint\limits_{S_{monopile}} p\left[\left(z-z_0\right)n_x - \left(x-x_0\right)n_z\right]dS\,, \tag{14}$$

in which $n = (n_x, n_y, n_z)$, $F = (F_x, F_y, F_z)$, (x_0, y_0, z_0) is the rotational center defined to be the monopile center at the seabed, i.e., (0 m, 0 m, -1 m). $S_{monopile}$ denotes the wet surface of the OWT monopile.

2.3. Model validation

In the present study, the geometric parameters of the HOBEM model are the same as those of the experimental model, as seen in figure 3. The outer and inner radii of the damping layer, as shown in Fig. 5(b), are set to be $r_1 = 2\lambda$ and $r_0 = \lambda$, respectively. The parameters of the incident waves are listed in Table 2. After convergent tests, the numbers of the computational elements on the free surfaces outside and inside the OWC chamber and monopile surface are taken to be 552, 168 and 240 respectively. The time step is specified to be T/100. In order to reproduce the hydrodynamic properties of the OWC integrated system, the artificial and nonlinear pneumatic damping coefficients are chosen as μ_1 =0.07 and μ_2=1.65, respectively.

Fig. 6 and Fig. 7 show the time series of the surface elevation at G_3 and air pressure P_{air} in the chamber, respectively. Two dimensionless wave numbers, i.e. kh=1.99 and 2.42, are selected in the plots. It can be seen that the simulated and measured results agree well with each other. Both the free surface and air pressure can be observed the periodic variations over a long period. Fig. 8 presents the time history of the hydrodynamic pressures at different measuring points, as indicated in Fig. 3, at kh=1.99. The superscript c denotes the corresponding results on the isolated OWT monopile. The predicted hydrodynamic pressures on the OWC shell and OWT monopile show good agreements with the experimental results. It should be noted that the experimental data at test point P_7 was not included in this study due to the accident fault of the proposed pressure sensor. From the figure, it is clear that relatively large pressure amplitudes occur at test points P_1, P_4, P_7 and P_{10}, which are close to the free surface. The same phenomenon was also reported in the experimental study of a land-based OWC device (Ning et al., 2016).

The averaged relative errors $\overline{\sigma}=\left|\overline{N_{w,\exp}}-\overline{N_{w,num}}\right|/\overline{N}_{w,\exp}\times 100\%$ between the predicted and measured chamber surface elevation, air pressure and point pressure are shown in Table 3 and Table 4, respectively. $\overline{N_w}$ denotes the peak value of both predicted and measured results. Due to the effect of vortex shedding induced by the OWC shell, the relative errors of the pressure are larger at the test points S_{10}, S_{11} and S_{12} than others. Overall, the numerical simulations are in a good agreement with the experiments for the test cases. Fig. 9 shows the variations of the crest amplitude of the surface elevation η_{crest} at G_3, the air pressure ΔP_{air} ($\Delta P_{air}=\left[P(t)_{air\max}-P(t)_{air\min}\right]/2$) and the hydrodynamic efficiency ξ with the dimensionless wave number kh. The wave frequency varies in the range of $1\leqslant kh\leqslant 3$ with the same wave steepness kA=0.05. The results demonstrate that the amplitude of the surface elevation, the air pressure and the hydrodynamic efficiency exhibit similar variation with kh. The resonant frequency occurs at kh=2.2, which leads to a piston-type resonant phenomenon with maximum hydrodynamic efficiency of 52% and has ever been revealed in the previous theoretical research (Zhou et al., 2018). In summary, the present numerical results are all in close agreement with the experiments, verifying the suitability of the present HOBEM model.

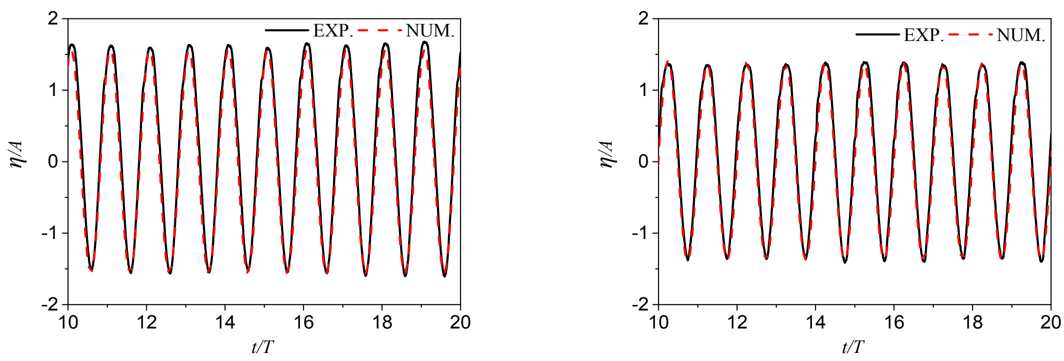

(a) (b)

Fig. 6. Time series of the simulated and measured surface elevations at G_3: (a) kh=1.99 and (b) kh=2.42.

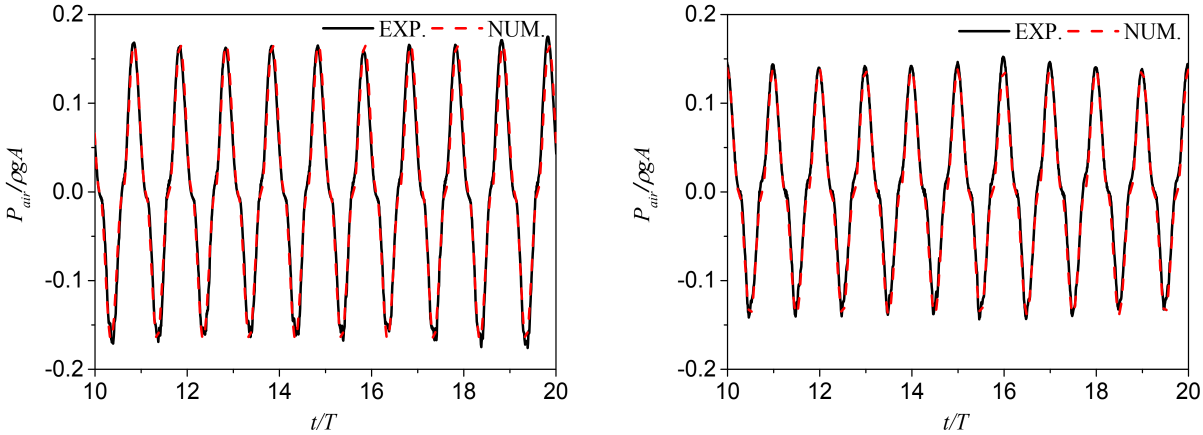

(a) (b)

Fig. 7. Time series of the simulated and measured air pressure in the chamber: (a) kh=1.99 and (b) kh=2.42.

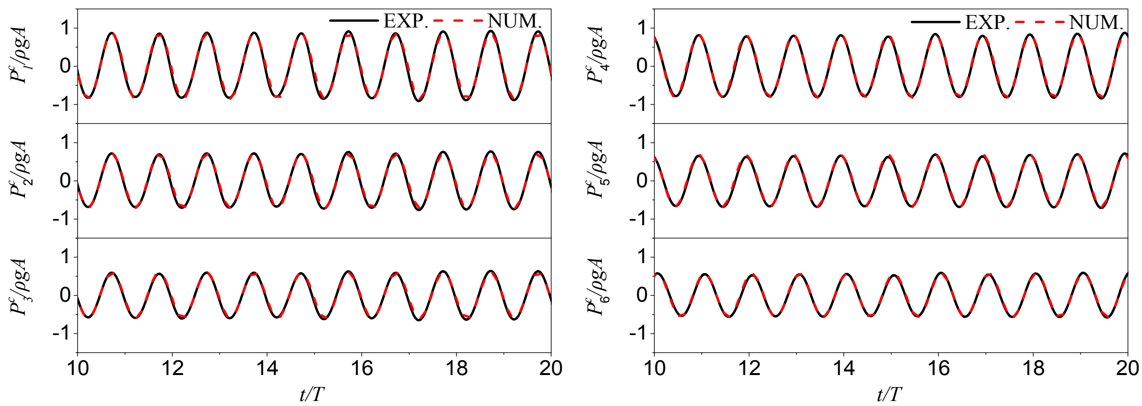

(a) At points S_1, S_2 and S_3 without OWC shell (b) At points S_4, S_5 and S_6 without OWC shell

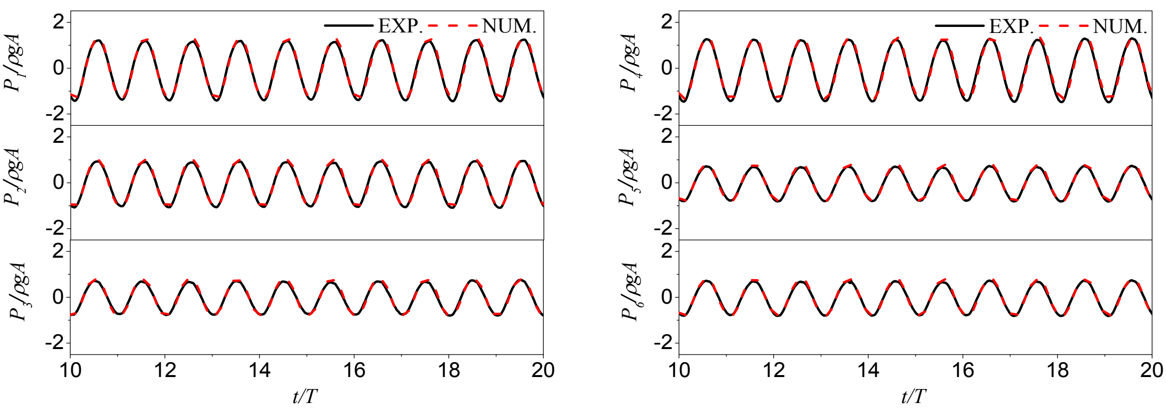

(c) At points S_1, S_2 and S_3 with OWC shell (d) At points S_4, S_5 and S_6 with OWC shell

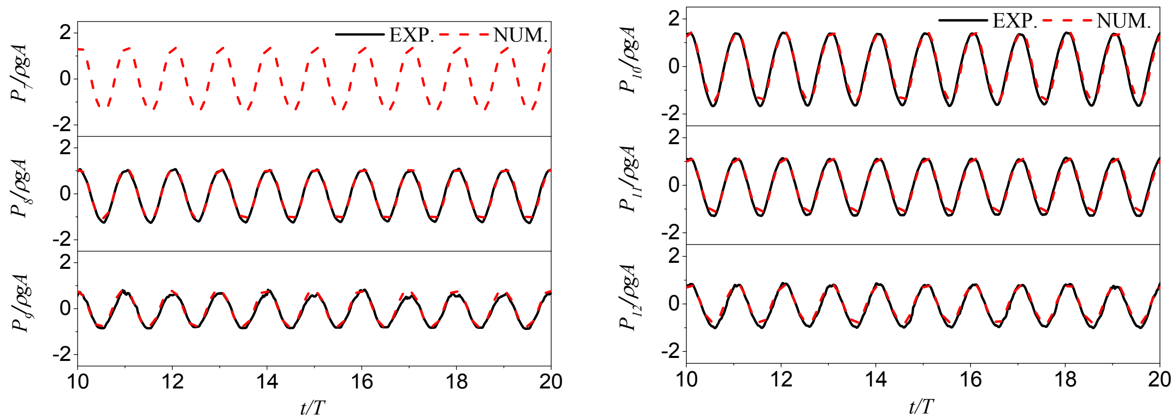

(e) At points S_7, S_8 and S_9 (f) At points S_{10}, S_{11} and S_{12}

Fig. 8. Comparisons of the simulated and measured pressures at different measuring points for *kh*=1.99.

Table 3 Averaged relative error between measured and predicted chamber surface elevation and air pressure at the test points. (%)

Position	G_3	$\overline{S_a}$
$\overline{\sigma}_{(kh=1.99)}$	2.22	0.1
$\overline{\sigma}_{(kh=2.42)}$	2.83	1.82

Table 4 Averaged relative error between measured and predicted pressure at the test points at *kh*=1.99. (%)

Position	S_1	S_2	S_3	S_4	S_5	S_6	S_8	S_9	S_{10}	S_{11}	S_{12}
$\overline{\sigma}$ (without OWC shell)	2.35	0.5	4.7	0.7	1.28	1.26					
$\overline{\sigma}$ (with OWC shell)	1.78	1.27	6.7	1.19	5.69	4.0	7.13	0.1	10.9	5.61	5.63

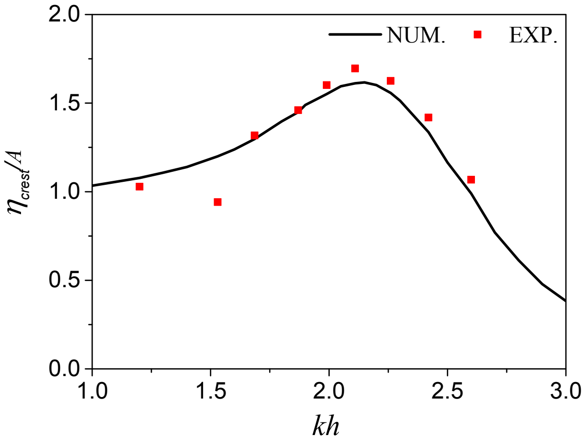

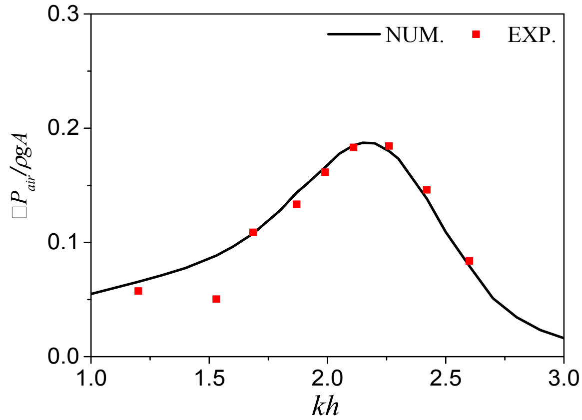

(a) surface elevation amplitude at G_3 (b) chamber air pressure amplitude

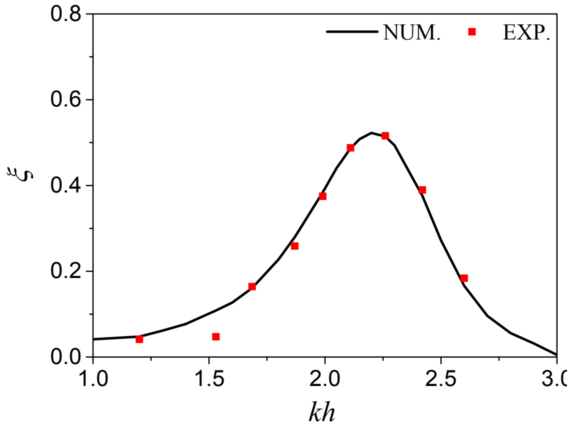

(c) hydrodynamic efficiency

Fig. 9. Distribution of the amplitudes of surface elevation and air pressure in the chamber and 5 hydrodynamic efficiency with the dimensionless wave number

3. Results and Discussions

3.1. Wave loads on the OWT monopile

In this section, the wave loads on the OWT monopile with different conditions are discussed. Fig. 10 illustrates the wave loads on the OWT monopile with and without the OWC chamber shell. The moment is about the rotational center point (0m, 0m, -1m). From the figure, it can be seen that the non-dimensional horizontal force $F_x/\rho gAD_c^2$ and overturning moment $M/\rho gAhD_c^2$ both significantly reduce with the introduction of the OWC shell, especially for the high-frequency waves. It is due to the OWC shell redistributes the wave potential around the OWT monopile to reduce the wave loads. Besides, the viscous drag and flow separation may also be generated around the thin OWC chamber, also contributing to the reduction of the wave loads. For short waves, they can be easily reflected by the large OWC shell, which leads to further reduction of wave loads on the OWT monopile in the high-frequency region.

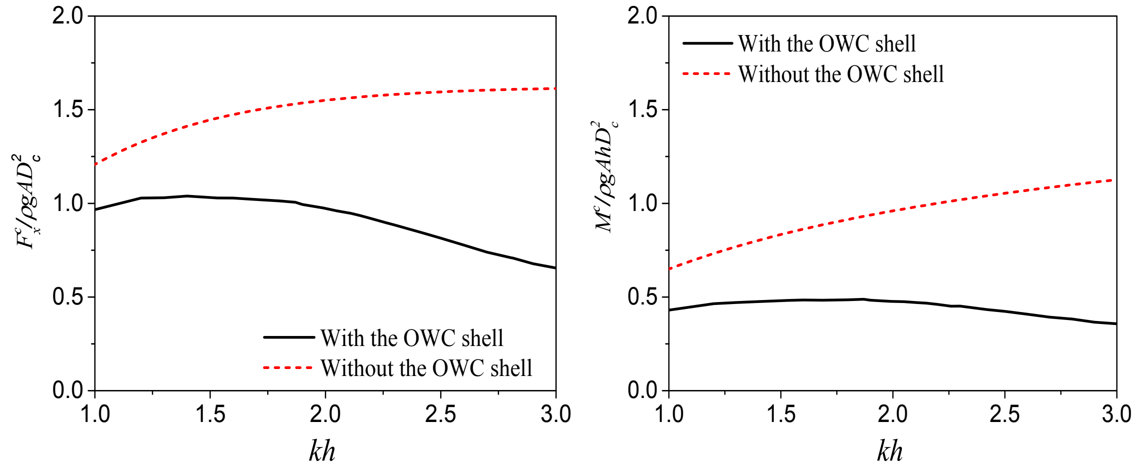

(a) Horizontal force (b) Overturning moment

Fig. 10. Wave loads on the OWT monopile versus dimensionless wave number *kh*.

3.2. Effects of turbine damping

In order to investigate the influence of turbine damping on the hydrodynamic response of the OWC chamber, three different nonlinear pneumatic damping coefficients are considered, i.e., μ_2=0.45, 1.65 and 2.85. The main geometric parameters of the OWC integrated system are set as R_1=0.1m, R_2=0.4m, d=0.3m, d_c=0.2m and the wave steepness is kept to be kA=0.05. Fig. 11 demonstrates the influence of the turbine damping on the non-dimensional amplitudes of the surface elevation η/A at G_3, the air pressure $\triangle P_{air}/\rho gA$ and the hydrodynamic efficiency ξ. From the figure, it can be seen that the PTO damping has a significant influence on both the surface elevation η and air pressure $\triangle P_{air}$ at the resonant frequency (kh=2.2). Such a behaviour has also been found in a small-scale experimental study of a floating cylindrical OWC device (Sheng et al., 2012). The air pressure increases and the surface elevation decrease with the pneumatic coefficient μ_2 increasing. From Fig. 11(c), it can be concluded that the maximal hydrodynamic efficiency is achieved at the resonant frequency regardless of the value of the pneumatic coefficient μ_2, which is varied from 0.45 to 2.85 in this study. It can be apparently seen that the effective frequency bandwidth broadens with the increase of the pneumatic coefficient μ_2, which benefits the power generation in the irregular wave state. Besides, the dimensionless surface elevation amplitude is close to unity in the low-frequency region in Fig.11(a), which means that the effect of long wave is more apparent than the turbine damping (Zhou et al., 2018). And the air pressure ΔP_{air} increases as the coefficient μ_2 increases in the low-frequency region. Therefore, it is possible to enhance the hydrodynamic efficiency in the low-frequency region by raising the turbine damping.

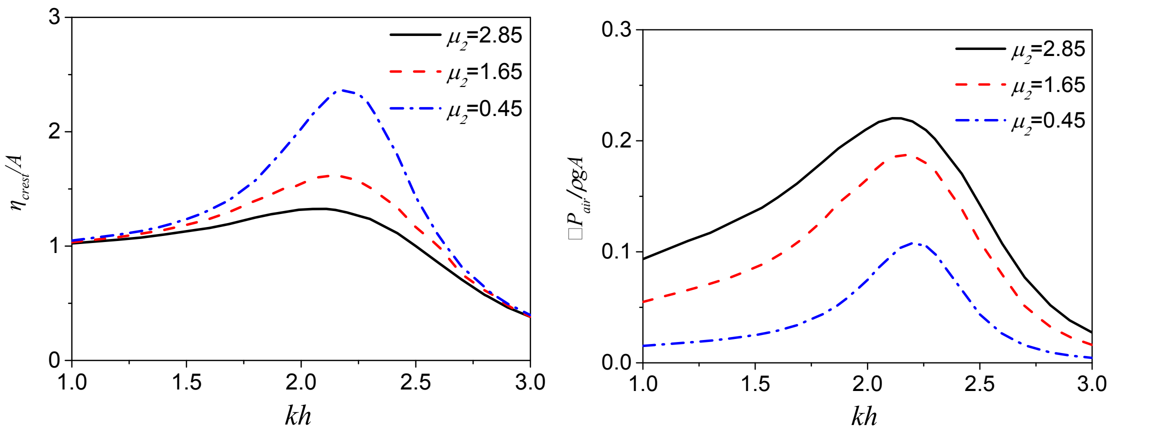

(a) Amplitude of the surface elevation at G_3 (b) Amplitude of the chamber air pressure

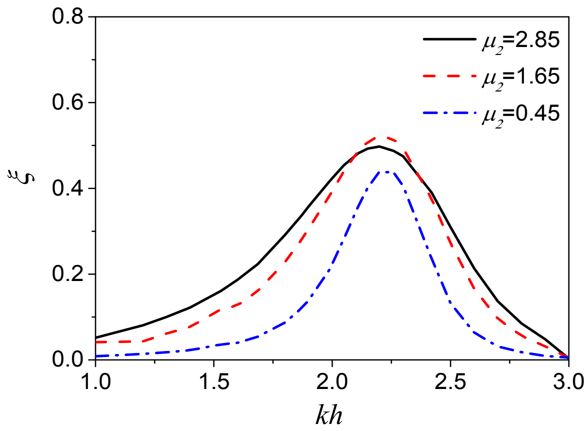

(c) Hydrodynamic efficiency

Fig. 11. Effects of the turbine damping on the hydrodynamic properties of the OWC chamber.

The wave dynamics on the OWT monopile is further investigated. Fig. 12 displays the variation of pressure at the points S_1 and S_4 with the pneumatic coefficient μ_2. The curve of pressure amplitude versus *kh* shows a similar trend to that of the surface elevation in Fig. 11(a). The resonant frequency also occurs at *kh*=2.2. It can be concluded that the pressure on the device is correlated with the free-surface motion in the chamber. The OWC system with larger turbine damping can reduce the local pressure on both the OWC shell and monopile. To further illustrate the pressure distribution on the OWT monopile, Fig. 13 shows the effects of the turbine damping on the non-dimensional pressure distribution $\triangle P/\rho gA$ along the seaside of the OWT monopile at resonant frequency (*kh*=2.2). It is clear that a huge pressure drops (at least 65%) occur under the relative water depth *z/h*=0.4. It illustrates that the wave energy is mainly concentrated on the fluid domain nearby the free surface. From Fig 13, it can be seen that the drop rate of the pressure increases with the decrease of the turbine damping μ_2 at the resonant frequency. This is due to the increase of the chamber surface elevation, which is greatly connected with the turbine damping μ_2 shown in Fig 11(a).

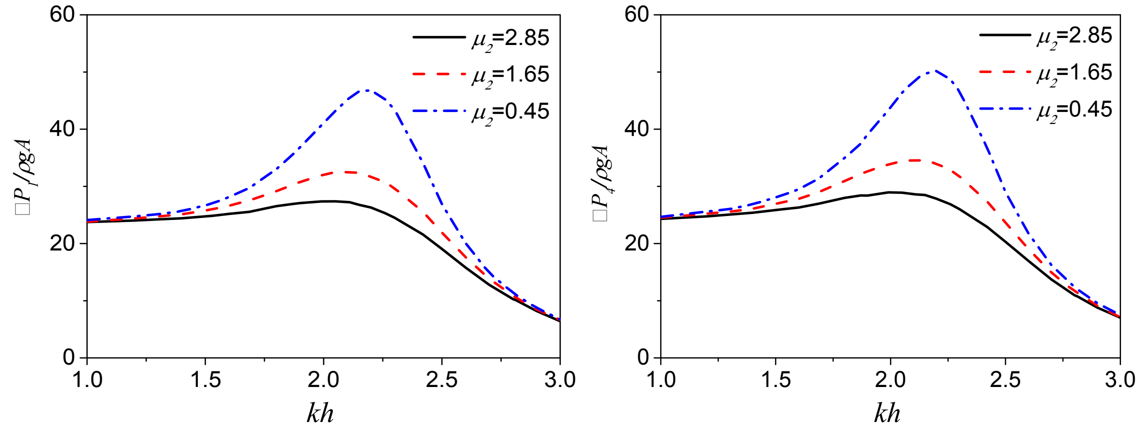

(a) (b)

Fig. 12. Effects of the turbine damping on the pressures of test points (a) P_1 and (b) P_4.

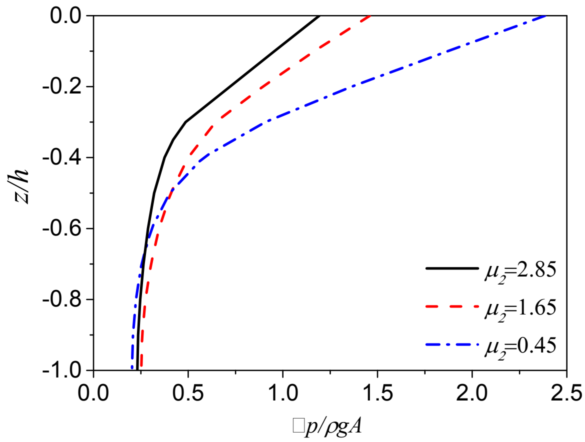

Fig. 13. Effects of the turbine damping on the pressure distribution along the seaside of the OWT monopile.

3.3. Effects of wave steepness

In this section, the nonlinear effects on the hydrodynamic performance of the OWC chamber are experimentally investigated under different wave steepness. The experiments are considered with four different wave steepness (*kA*=0.05, 0.075, 0.10 and 0.15) and four different wave conditions (*kh*=2.6, 2.26, 2.11 and 1.99), as shown in Table 2. Fig. 14 shows the hydrodynamic efficiency of the OWC device versus the wave steepness *kA*. As the wave steepness *kA* increases, the hydrodynamic efficiency generally decreases, especially near the resonant frequency (*kh*=2.2). As the wave steepness *kA* increases from 0.05 to 0.15, the hydrodynamic efficiency of the OWC device reduces by 16.6% at kh=2.26. The same phenomenon was ever found in the land-fixed OWC devices (López et al., 2015). The reason is due to higher harmonics with more energy transferred from the fundamental wave easily reflected by the chamber external shell in the case of stronger nonlinear waves.

To further illustrate the physics in detail, the non-dimensional amplitudes of the surface elevation η_{crest}/A at G_3 and the air pressure $\triangle P_{air}/\rho gA$ are presented in Fig. 15. The dimensionless surface elevation η_{crest}/A inside the chamber decreases greatly with the increase of wave steepness kA, especially in the resonant region. As kA increases from 0.05 to 0.15, the dimensionless surface elevation η_{crest}/A reduces by 39.7% at kh=2.26, which is larger than that (21.9%) at kh=2.6. It should be noted that η_{crest}/A denotes a relative value normalized by the incoming wave amplitude. To further analyze the nonlinear effects on the chamber free-surface-elevation, the results of the spectral frequency analysis at the test point G_3 for different wave steepness kA are shown in Fig. 16. From the figure, it can be seen that fundamental and second-order waves occur in the chamber, but the fundamental waves are the dominant. Furthermore, the dimensionless amplitude of the fundamental wave decrease with the increase of the wave steepness kA. It further illustrates the stronger reflection of the OWC chamber shell for the higher harmonic waves, which lead to a smaller dimensionless surface elevation η_3/A. Fig. 15(b) shows the variations of the dimensionless air pressure versus the wave steepness kA. Compared with the dimensionless surface elevation amplitude in Fig. 15(a), the dimensionless air pressure amplitude follows an opposite trend with the wave steepness kA. Elhanafi and Chan (2018) also observed that the dimensionless air pressure increases with the wave height over the entire frequency range. This result can be attributed to the surface variation rate $(\eta_{max(t)}-\eta_{min(t)})/T$, which increases with the wave steepness kA and thus the compression rate of the pneumatic air inside the OWC chamber increases. The air pressure inside the chamber increases by 18.4% as kA increases from 0.05 to 0.15 at kh = 2.26. However, the dimensionless surface elevation η_{crest}/A inside the chamber decreases more at the same conditions, which leads to the decrease of the hydrodynamic efficiency.

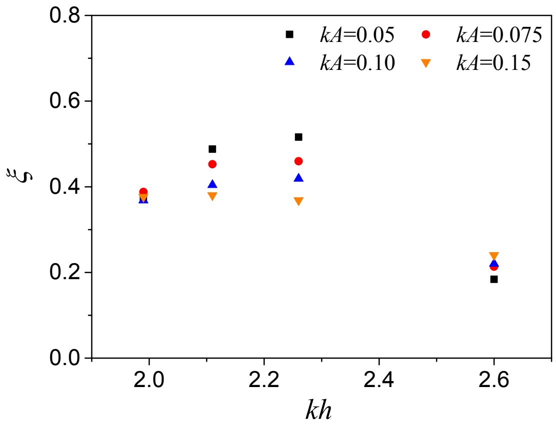

Fig. 14. Effects of the wave steepness kA on the hydrodynamic efficiency.

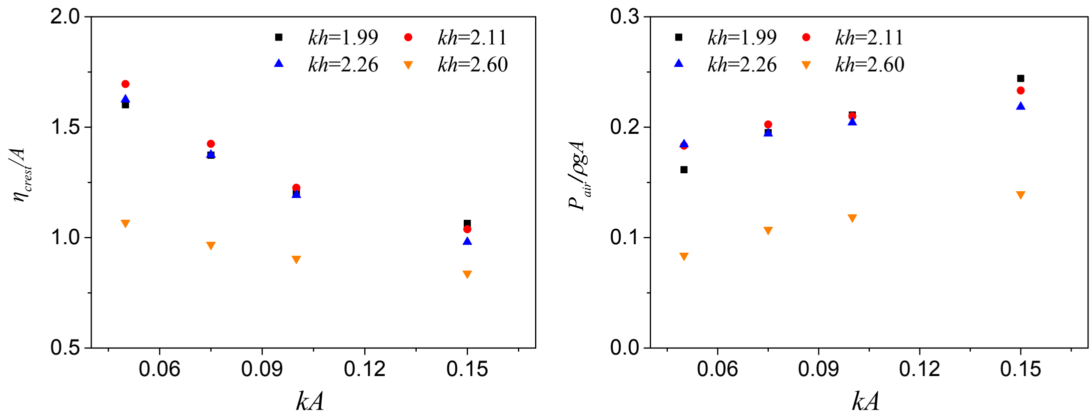

(a) (b)

Fig. 15. Effects of the wave steepness kA on the (a) surface elevation η at G_3 and (b) chamber air pressure $\triangle P_{air}$.

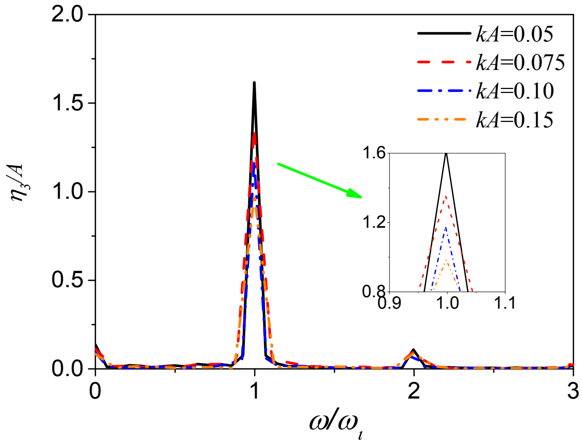

Fig. 16. Spectral frequency analysis of the chamber free surface elevation η_3 at kh=2.26.

4. Conclusions

In the present study, the hydrodynamic performance of an OWC wave energy converter integrated into a fixed OWT monopile was investigated numerically and experimentally. The OWC device is able to not only absorb the wave energy, but also reduce wave loads on the OWT monopile. Based on linear potential flow theory, a 3D time-domain HOBEM model is applied to simulate the OWC integrated system. The numerical results show good agreement with the experimental data. The hydrodynamic performance of the OWC integrated system is further investigated, especially the effects of the turbine damping and wave steepness.

The wave loads on the OWT monopile with or without the OWC chamber are discussed. The OWC chamber shell can reduce the horizontal force and overturning moment on the monopile. The PTO damping has a significant influence on the free surface elevation, the air pressure in the chamber and the hydrodynamic efficiency. The wave steepness has a significant influence on the hydrodynamic efficiency, especially near the resonant frequency. An increase in the wave steepness results in a decrease of the nondimensional surface elevation in the chamber and an increase of the chamber air pressure.

The present study neglects the effects of extreme waves, which often occur in the ocean. In evaluating the reliability and viability of the device, the extreme wave load is a key parameter. Therefore, future work will focus on the effects of irregular and extreme waves on the complete system.

Acknowledgements

This work is supported by the National Key R&D Program of China (Grant No. 2018YFB151905), National Natural Science Foundation of China (Grant Nos. 51679036 and 51761135011) and EPSRC (Grant No. EP/R007519/1).

References

Achmus, M., Kuo, Y.S., Abdel-Rahman, K., 2009. Behavior of monopile foundations under cyclic lateral load. Computers and Geotechnics 36, 725-735.

Aemesto, I., Guanche, R., Alvar, J.A.A., Alves, M.A., Vidal, C., Losada, I., 2014. Time-domain modeling of a fixed detached oscillating water column towards a floating multi-chamber device. Ocean Eng. 76, 65-74.

Bahaj, A.B.S., 2011. Generating electricity from the oceans. Renewable Sustainable Energy Reviews 15, 3399-3416.

Bai, W., Teng, B., 2013. Simulation of second-order wave interaction with fixed and floating structures in time domain. Ocean Eng. 74, 168-177.

Chen, L., Stagonas, D., Santo, H., Buldakov, E., Simons, R., Taylor, P., Zang, J., 2019. Numerical modelling of interactions of waves and sheared currents with a surface piercing vertical cylinder. Coast. Eng. 145, 65-83.

Cheng, Z., Wen, T.R., Ong, M.C., Wang, K., 2019. Power performance and dynamic responses of a combined floating vertical axis wind turbine and wave energy converter concept. Energy 171, 190-204.

da Fonseca, F.C., Gomes, R., Henriques, J., Gato, L., Falcao, A., 2016. Model testing of an oscillating water column spar-buoy wave energy converter isolated and in array: Motions and mooring forces. Energy 112, 1207-1218.

Elhanafi, A., Chan, J.K., 2018. Experimental and numerical investigation on wave height and power take–off damping effects on the hydrodynamic performance of an offshore–stationary OWC wave energy converter. Renew. Energy 125, S0960148118302830.

Elhanafi, A., Macfarlane, G., Fleming, A., Zhi, L., 2017. Investigations on 3D effects and correlation between wave height and lip submergence of an offshore stationary OWC wave energy converter. Appl. Ocean Res. 64, 203-216.

Falcão, A.F., Henriques, J.C., Gato, L.M., Gomes, R.P., 2014. Air turbine choice and optimization for floating oscillating-water-column wave energy converter. Ocean Eng. 75, 148-156.

Falcão, A.F.O., Henriques, J.C.C., 2016. Oscillating-water-column wave energy converters and air turbines: A review. Renew. Energy 85, 1391-1424.

Ferrant, P., 1993. Threedimensional Unsteady Wave-Body Interactions by a Rankine

Boundary Element Method. Ship Technology Research 40, 165-175.

Gomes, R.P.F., Henriques, J.C.C., Gato, L.M.C., Falcão, A.F.O., 2016. Wave power extraction of a heaving floating oscillating water column in a wave channel. Renew. Energy 99, 1262-1275.

Haji, M.N., Kluger, J.M., Sapsis, T.P., Slocum, A.H., 2018. A symbiotic approach to the design of offshore wind turbines with other energy harvesting systems. Ocean Eng. 169, 673-681.

He, F., Leng, J., Zhao, X., 2017. An experimental investigation into the wave power extraction of a floating box-type breakwater with dual pneumatic chambers. Appl. Ocean Res. 67, 21-30.

He, F., Zhang, H., Zhao, J., Zheng, S., Iglesias, G., 2019. Hydrodynamic performance of a pile-supported OWC breakwater: An analytical study. Appl. Ocean Res. 88, 326-340.

Heath, T.V., 2012. A review of oscillating water columns. Philosophical Transactions of the Royal Society London 370, 235-245.

Jin, R., Teng, B., Ning, D., Zhao, M., Cheng, L., 2017. Numerical investigation of influence of wave directionality on the water resonance at a narrow gap between two rectangular barges. Acta Oceanologica Sinica 36, 104-111.

Kim, Y., 2003. Artificial Damping In Water Wave Problems I: Constant Damping. Int. J. Offshore Polar 13.

Koo, W., Kim, M.H., 2010. Nonlinear Time-Domain Simulation of a Land-Based Oscillating Water Column. Journal of Waterway Port Coastal Ocean Engineering 136, 276-285.

Liang, L., Yan, G., Yuan, Z., Day, S., Hu, Z., 2017. Dynamic response and power production of a floating integrated wind, wave and tidal energy system. Renew. Energy 116, S0960148117309217.

López, I., Pereiras, B., Castro, F., Iglesias, G., 2015. Performance of OWC wave energy converters: influence of turbine damping and tidal variability. International Journal of Energy Research 39, 472-483.

Mahnamfar, F., Altunkaynak, A., 2017. Comparison of numerical and experimental analyses for optimizing the geometry of OWC systems. 130, 10-24.

Medina-Lopez, E., Ferrando, A.M., Gilabert, M.C., Pino, C.d., Rodríguez, M.L., 2016. Note on a real gas model for OWC performance. Renew. Energy 85, 588-597.

Michailides, C., Gao, Z., Moan, T., 2016. Experimental study of the functionality of a semisubmersible wind turbine combined with flap-type Wave Energy Converters. Renew. Energy 93, 675-690.

Morris-Thomas, M.T., Irvin, R.J., Thiagarajan, K.P., 2007. An investigation into the hydrodynamic efficiency of an oscillating water column. Journal of Offshore Mechanics and Arctic Engineering 129, 273-278.

Ning, D.-z., Zhou, Y., Mayon, R., Johanning, L., 2020. Experimental investigation on the hydrodynamic performance of a cylindrical dual-chamber Oscillating Water Column device. Appl. Energy 260, 114252.

Ning, D., Zhou, Y., Zhang, C., 2018. Hydrodynamic modeling of a novel dual-chamber OWC wave energy converter. Appl. Ocean Res. 78, 180-191.

Ning, D.Z., Shi, J., Zou, Q.P., Teng, B., 2015. Investigation of hydrodynamic performance of an OWC (oscillating water column) wave energy device using a fully nonlinear HOBEM (higher-order boundary element method). Energy 83, 177-188.

Ning, D.Z., Wang, R.Q., Chen, L.F., Sun, K., 2019. Experimental investigation of a land-based dual-chamber OWC wave energy converter. Renew. Sust. Energ. Rev. 105, 48-60.

Ning, D.Z., Wang, R.Q., Ying, G., Ming, Z., Teng, B., 2016. Numerical and experimental investigation of wave dynamics on a land-fixed OWC device. Energy 115, 326-337.

Ohlenforst, K., Council, G.W.E., 2019. Global Wind Report 2018. Recuperado.

Paulsen, B.T., Sonneville, B.d., Meulen, M.v.d., Jacobsen, N.G., 2019. Probability of wave slamming and the magnitude of slamming loads on offshore wind turbine foundations. Coast. Eng. 143, 76-95.

Pechak, O., Mavrotas, G., Diakoulaki, D., 2011. Role and contribution of the clean development mechanism to the development of wind energy. Renewable Sustainable Energy Reviews 15, 3380-3387.

Perez-Collazo, C., Greaves, D., Iglesias, G., 2018. Hydrodynamic response of the WEC sub-system of a novel hybrid wind-wave energy converter. Energy Convers. Manage. 171, 307-325.

Pérez-Collazo, C., Greaves, D., Iglesias, G., 2015. A review of combined wave and offshore wind energy. Renewable Sustainable Energy Reviews 42, 141-153.

Perez-Collazo, C., Richard, P., Greaves, D., Iglesias, G., 2019. Monopile-mounted wave energy converter for a hybrid wind-wave system. Energy Convers. Manage. 199, 111971.

Ren, N., Zhe, M., Fan, T., Zhai, G., Ou, J., 2018. Experimental and numerical study of hydrodynamic responses of a new combined monopile wind turbine and a heave-type wave energy converter under typical operational conditions. Ocean Eng. 159, 1-8.

Rezanejad, K., Bhattacharjee, J., Soares, C.G., 2013. Stepped sea bottom effects on the efficiency of nearshore oscillating water column device. Ocean Eng. 70, 25-38.

Sarmiento, J., Iturrioz, A., Ayllón, V., Guanche, R., Losada, I.J., 2019. Experimental modelling of a multi-use floating platform for wave and wind energy harvesting. Ocean Eng. 173, 761-773.

Shalby, M., Elhanafi, A., Walker, P., Dorrell, D.G., 2019. CFD modelling of a small-scale fixed multi-chamber OWC device. Appl. Ocean Res. 99, 37-47.

Sheng, W., 2019. Wave energy conversion and hydrodynamics modelling technologies: A review. Renew. Sust. Energ. Rev. 109, 482-498.

Sheng, W., Alcorn, R., Lewis, A., 2013. On thermodynamics in the primary power conversion of oscillating water column wave energy converters. J. Renew. Sustain. Ener. 5, 1257-1294.

Sheng, W., Flannery, B., Lewis, A., Alcorn, R., 2012. Experimental Studies of a Floating Cylindrical OWC WEC. In: 31st International Conference on Ocean, Offshore and Arctic Engineering, ASME 169-178. in Rio de Janeiro, Brazil.

Simonetti, I., Cappietti, L., Elsafti, H., Oumeraci, H., 2017. Optimization of the geometry and the turbine induced damping for fixed detached and asymmetric OWC devices: A numerical study. 139, 1197-1209.

Slot, R.M., Sørensen, J.D., Sudret, B., Svenningsen, L., Thøgersen, M.L., 2019. Surrogate model uncertainty in wind turbine reliability assessment. Renew. Energy.

Soares, C.G., 1995. Offshore structure modelling. World Scientific.

Wan, L., Gao, Z., Moan, T., 2015. Experimental and numerical study of hydrodynamic responses of a combined wind and wave energy converter concept in survival modes. Coast. Eng. 104, 151-169.

Wang, R.Q., Ning, D.Z., Zhang, C.W., Zou, Q.P., Liu, Z., 2018. Nonlinear and viscous effects on the hydrodynamic performance of a fixed OWC wave energy converter. Coast. Eng. 131, 42-50.

Wind-Europe,Wind Europe, 2019. Offshore Wind in Europe: Key Trends and Statistics 2018. Brussels, Belgium.

Wu, X., Hu, Y., Li, Y., Yang, J., Liao, S., 2019. Foundations of offshore wind turbines: A review. Renewable Sustainable Energy Reviews 104, 379-393.

Xu, C., Huang, Z., Deng, Z., 2016. Experimental and theoretical study of a cylindrical oscillating water column device with a quadratic power take-off model. Appl. Ocean Res. 57, 19-29.

Zheng, S., Antonini, A., Zhang, Y., Greaves, D., Miles, J., Iglesias, G., 2019. Wave power extraction from multiple oscillating water columns along a straight coast. J. Fluid Mech. 878, 445-480.

Zheng, S., Zhang, Y., Iglesias, G., 2018. Wave–structure interaction in hybrid wave farms. J. Fluid. Struct. 83, 386-412.

Zhou, Y., Zhang, C., Ning, D., 2018. Hydrodynamic Investigation of a Concentric Cylindrical OWC Wave Energy Converter. Energies 11, 985.